

Development of a Gray-Level Co-Occurrence Matrix-Based Texture Orientation Estimation Method and Its Application in Sea Surface Wind Direction Retrieval From SAR Imagery

Gang Zheng^{ID}, Xiaofeng Li^{ID}, Senior Member, IEEE, Lizhang Zhou, Jingsong Yang, Lin Ren,
Peng Chen^{ID}, Huaguo Zhang, and Xiulin Lou

Abstract—A gray-level co-occurrence matrix (GLCM)-based method was developed for better texture orientation estimation in remote sensing imagery. A GLCM is essentially the joint probability distribution of gray levels at the position pairs satisfying a specific relative position within an image. We first found that when the relative position is aligned with texture orientation, larger elements of the corresponding GLCM are concentrated diagonally. Then, we developed a new texture orientation estimation method. The method uses the GLCMs of relative positions equally spaced in orientation and distance, and three schemes of these GLCMs are calculated. A GLCM-derived parameter is then defined to quantitatively measure the degree of diagonal concentration of the GLCM elements, and its integral over the variable of relative distance is selected as an indicator to find the dominant texture orientation(s). For testing, we applied the method to 44 selected images containing one or multiple aligned textures. The results show that the method is in good agreement with visual inspections from 45 randomly selected people, and is insensitive to large typical noises and illumination change. In addition, using (any) one GLCM calculation scheme over the others does not significantly affect the results. Finally, the method was applied to sea surface wind direction (SSWD) retrieval from 89 synthetic aperture radar images. In the application test, the developed method achieves better SSWD retrieval accuracy than do the commonly used Fourier transform- and gradient-based methods by 8.13° and 16.09° against the European Centre for Medium-Range Weather Forecast ERA-Interim reanalysis data and 10.21° and 17.31° against the cross-calibrated multiplatform data.

Manuscript received October 30, 2017; revised January 16, 2018; accepted February 16, 2018. Date of publication April 4, 2018; date of current version August 27, 2018. This work was supported in part by the National Natural Science Foundation of China under Grant 41676167 and Grant 41306192, in part by the National Key Research and Development Program of China under Grant 2016YFC1401007, in part by the European Space Agency and the Ministry of Science and Technology Dragon 4 Cooperation Programme of China under Grant 32249, and in part by the Project of State Key Laboratory of Satellite Ocean Environment Dynamics, Second Institute of Oceanography, under Grant SOEDZZ1804. (*Corresponding author: Gang Zheng*)

G. Zheng, L. Zhou, J. Yang, L. Ren, P. Chen, H. Zhang, and X. Lou are with the State Key Laboratory of Satellite Ocean Environment Dynamics, Second Institute of Oceanography, State Oceanic Administration, Hangzhou 310012, China (e-mail: zhenggang@sio.org.cn).

X. Li is with the Center for Satellite Applications and Research, National Environmental Satellite, Data, and Information Service, NOAA, Global Science and Technology, Inc., College Park, MD 20740 USA.

Color versions of one or more of the figures in this paper are available online at <http://ieeexplore.ieee.org>.

Digital Object Identifier 10.1109/TGRS.2018.2812778

Index Terms—Gray-level co-occurrence matrix (GLCM), retrieval, sea surface, synthetic aperture radar (SAR), texture orientation, wind direction.

I. INTRODUCTION

TEXTURE is regarded as the human's impression of directionality, periodicity, and fineness of a surface, e.g., a weave of fabric, bark of a tree, and sea surface. Some of the definitions of texture are as follows.

- 1) Texture is the visual effect which is produced by spatial distribution of tonal variations over relatively small areas [1].
- 2) Texture images are spatially homogeneous and typically contain repeated structures, often (but not necessarily) with some random variations [2], [3].

As an innate property of visual surfaces [4], texture is an important topic that has been widely studied in many fields [5]–[11]. Among these, a lot of effort has been carried out to extract texture features in order to describe them objectively.

From image processing point of view, to derive the texture feature, Fourier transform (FT)-based and gradient-based methods are commonly used. These methods all have limitations affected by image noise among others. The gray-level co-occurrence matrix (GLCM) can be potentially used to overcome some of the shortcomings. The conventional GLCM is the joint probability distribution of gray levels of pixel pairs (satisfying a specific relative position) within an image. It can be estimated by counting pixel pairs in the image. Several second-order statistical parameters (e.g., energy and entropy) can then be extracted from the GLCMs, representing different features of textures [1], [4], [12]–[14]. Discrimination among textures depends mostly on their differences in second-order statistics [15], [16]; hence, the parameters are useful in the recognition, classification, and segmentation of an image.

Studies on human texture perception have indicated that orientation is an important texture feature naturally used in human texture perception [12], [17]. Texture orientation also has practical applications in various fields, such as remote sensing image analysis. This is because texture orientation

often indicates some information concerning a physical phenomenon. For example, sea surface wind streaks imaged by remote sensing instrument are directly related to the sea surface wind direction (SSWD). Wind is a basic force that drives the motions of atmosphere and ocean. Conventional way of measuring sea surface winds by ships and buoys has limitation in spatial coverage. However, much wider coverage and subkilometer resolution sea surface wind can be obtained through synthetic aperture radar (SAR) remote sensing imagery [18]–[26]. In order to calculate sea surface wind from SAR imagery, SSWD must be obtained first. The most popular way to retrieve SSWD from SAR imagery is based on oriented textures, which are considered to be associated and aligned with wind-induced streaks and marine atmospheric boundary layer rolls (usually due to boundary layer spanning eddies that have an orientation turned slightly away from the surface wind direction and also visible in optical sun glitter observations and satellite cloud imagery) [27]–[31]. In addition to sea surface winds, other ocean phenomena may also produce oriented textures in SAR or optical images, such as internal waves, surface imprints of sand waves, and ocean-surface waves [32]–[34]. Texture orientation estimation also has many applications in other fields, including interpretation of seismic [35] and medical [36] images, and assessment of machined surfaces in industry [37].

Several methods have been developed for texture orientation estimation including most commonly used spectrum-based and gradient-based methods. The FT-based method is a typical spectrum-based one for such purpose [27], [29], [31], [37], [38]. It is based on the fact that the Fourier spectrum of an image with an oriented texture is concentrated along a line perpendicular to the texture orientation [39], [40]. This method usually requires a large rectangular data set with many samples of the texture to accurately calculate the Fourier spectrum [40]. Other similar spectrum-based methods have also been developed, including those based on the Radon transform [41], the Gabor filter [42], [43], and the wavelet transform [44]. For gradient-based methods, local orientation of a texture is estimated by assuming that it is perpendicular to the image intensity gradient [45]–[50]. However, this estimation is OFF in the areas near the extrema of the image intensity, where the magnitude of the gradient is very small [48]. A solution to this problem was proposed by introducing a valleyness operator for the areas. The gradient and valleyness operators were then optimized for bias reduction by using the Taylor series expansion [48]. Gradients of images are commonly calculated with difference approximations in the gradient-based methods like Sobel operator that is easily affected by noise. Thus, smoothing image and calculating gradient are combined in the frequency domain to reduce the noise influence [50]. Texture orientation can also be estimated from autocorrelation functions of oriented texture images [40], [51]; the relationship between gradient vectors and autocorrelation functions was examined in [51]. The FT- and gradient-based methods are commonly used in SSWD retrieval from SAR imagery. However, as mentioned above, the requirement of a large rectangular data set with many wind-induced texture samples (to accurately calculate the

Fourier spectrum) limits spatial resolution, and the difference approximations to calculate image gradient are susceptible to noise.

GLCM-based texture analysis does not have the above issues of the FT- and gradient-based methods. To our knowledge, although GLCM was proposed several decades ago, its potential for texture orientation estimation has not been systematically explored in the literature. One reason is that the conventional method of calculating GLCMs is limited by the positions of pixels in images. Typically, GLCMs are calculated at angles of 90° , 45° , 0° , and -45° with respect to the horizontal (i.e., the x -axis in Fig. 1). In reality, the orientation of texture may not occur at these angles. Therefore, the GLCMs at these limited angles are usually insufficient to resolve texture orientation. In this paper, a GLCM-based texture orientation estimation method was proposed, using the GLCMs of relative positions equally spaced in terms of orientation and distance. The entire procedure of the method is simple and straightforward. This new method was found to be consistent with human visual inspection and insensitive to large typical noises and illumination change in the tests reported in this paper.

The rest of this paper is organized as follows. In Section II, the procedure of the novel texture orientation estimation method is presented along with the three GLCM calculation schemes. In Section III, the proposed method with different GLCM calculation schemes is tested using 44 images containing different textures. The results are cross compared and also inspected by 45 randomly selected people for visual check. In Section IV, the method is applied to retrieve SSWDs from 89 SAR images. The results are validated against the European Centre for Medium-Range Weather Forecast (ECMWF) ERA-Interim reanalysis data [52] and the cross-calibrated multiplatform (CCMP) data [53]. Comparisons are also made with the existing FT- and gradient-based methods. Finally, a summary is given in Section V.

II. PROCEDURE OF TEXTURE ORIENTATION ESTIMATION

A. GLCM Calculation Schemes

An asymmetrical GLCM is essentially a joint probability distribution of gray levels at the position pairs satisfying a specific relative position within an image. Without loss of generality, let us assume that the gray-level range of an image varies from 0 to $N - 1$. Then, the GLCM is an $N \times N$ matrix. In the conventional GLCM analysis, only the GLCMs of relative positions are used, which can coincide with pixels in the image. For a GLCM of relative position (r, θ) coinciding with the pixels, its matrix element (m, n) can be calculated by counting the pixel pairs as follows [8]:

$$G(m, n; r, \theta) = \frac{\text{card} \left\{ \begin{array}{l} (i, j) | f(i, j) = m - 1, \\ f(i + r \cos \theta, j + r \sin \theta) = n - 1, \\ (i, j) \in \mathcal{P}, (i + r \cos \theta, j + r \sin \theta) \in \mathcal{P} \end{array} \right\}}{Q(r, \theta)} \quad (1)$$

where “card” denotes the number of elements in a set. r represents the distance between the two ends of the relative position,

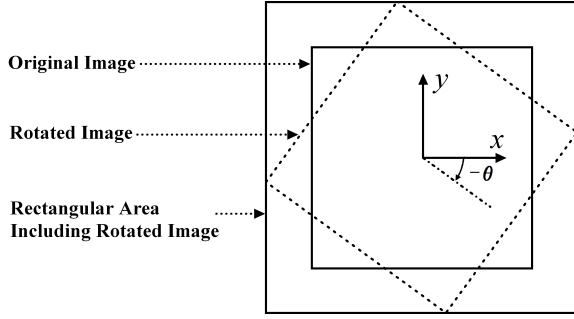


Fig. 1. Geometry of scheme 1 of GLCM calculation.

and θ represents the orientation of the relative position in terms of the (counterclockwise) angle with respect to the horizontal orientation of the image (i.e., the x -axis in Fig. 1). \mathcal{P} represents the pixel set of the image. $f(x, y)$ is the gray level at position (x, y) in the rectangular coordinate system (shown in Fig. 1). Pixel spacing is adopted as distance unit in this paper. The normalization factor $Q(r, \theta)$ is

$$Q(r, \theta) = \text{card}\{(i, j) | (i, j) \in \mathcal{P}, (i + r \cos \theta, j + r \sin \theta) \in \mathcal{P}\}. \quad (2)$$

Equation (2) represents the number of pixel pairs, which satisfy the relative position (r, θ) . Typically, $G(m, n; r, -45^\circ)$, $G(m, n; r, 0^\circ)$, $G(m, n; r, 45^\circ)$, and $G(m, n; r, 90^\circ)$ are used in the conventional GLCM analysis. However, these specific GLCMs are insufficient for texture orientation estimation because the texture may not be oriented at these angles. Moreover, for GLCMs calculated using (1), the distances (r) of the relative positions are not always the same at different angles. For instance, the distances at 0° are given by integer times pixel spacing, but those at 45° are given by integer times $\sqrt{2}$ pixel spacing. Thus, three GLCM calculation schemes are presented below. These schemes can be used to calculate the GLCMs of arbitrary relative positions, and are used in the proposed texture orientation estimation method described in Section II-B to calculate the GLCMs of relative positions equally spaced in distance (r) and orientation (θ).

1) *Scheme 1:* Scheme 1 is based on image rotation as shown in Fig. 1. If $G(m, n; r, \theta)$ of an image is to be calculated [where the relative position (r, θ) can be arbitrary], we can rotate the image by angle $-\theta$. Then, $G(m, n; r, \theta)$ can be calculated from the rotated image as follows:

$$G(m, n; r, \theta) = (\lfloor r \rfloor + 1 - r) \times G'(m, n; \lfloor r \rfloor, 0^\circ) + (r - \lfloor r \rfloor) \times G'(m, n; \lfloor r \rfloor + 1, 0^\circ) \quad (3)$$

where “ $\lfloor \bullet \rfloor$ ” denotes rounding down. $G'(m, n; \lfloor r \rfloor, 0^\circ)$ and $G'(m, n; \lfloor r \rfloor + 1, 0^\circ)$ are elements (m, n) of the GLCMs of the rotated image of the relative positions $(\lfloor r \rfloor, 0^\circ)$ and $(\lfloor r \rfloor + 1, 0^\circ)$, respectively. The relative positions $(\lfloor r \rfloor, 0^\circ)$ and $(\lfloor r \rfloor + 1, 0^\circ)$ can coincide with the pixels. For relative position (r', θ') that coincides with the pixels, its corresponding GLCM of the rectangular area (including the rotated image, shown in Fig. 1) can be directly calculated using (1) and letting \mathcal{P} be the set of the pixels in the rectangular area. To obtain the GLCM of the rotated image (dashed-line box) from the rectangular area (bigger solid-line box), the effects of the

four corners (i.e., the parts of the rectangular area outside the rotated image in Fig. 1) should be removed. This can be easily done as shown below. For convenience, we let the gray level of the corners be N . Then, the GLCM of the rotated image is the block of the GLCM of the rectangular area from row 1 to N and from column 1 to N .

In the texture orientation estimation method described in Section II-B, distance r can be set to integer times pixel spacing. Then, (3) is simplified to

$$G(m, n; r, \theta) = G'(m, n; r, 0^\circ). \quad (4)$$

2) *Scheme 2:* The relative position (r, θ) of $G(m, n; r, \theta)$ may not coincide with pixels in the image. As a result, (1) is not always applicable. However, we can always find $(r_1, \theta_1), \dots, (r_K, \theta_K)$ in the neighborhood of (r, θ) , which coincide with the pixels. Thus, the GLCMs of $(r_1, \theta_1), \dots, (r_K, \theta_K)$ can be directly calculated using (1). Finally, $G(m, n; r, \theta)$ can be obtained by the interpolation of $G(m, n; r_1, \theta_1), \dots, G(m, n; r_K, \theta_K)$.

If we use bilinear interpolation, $G(m, n; r, \theta)$ can be calculated using

$$G(m, n; r, \theta) = c_1 \times G(m, n; r_1, \theta_1) + c_2 \times G(m, n; r_2, \theta_2) + c_3 \times G(m, n; r_3, \theta_3) + c_4 \times G(m, n; r_4, \theta_4) \quad (5)$$

where

$$\begin{aligned} G(m, n; r_1, \theta_1) &= G(m, n; \lfloor r \cos \theta \rfloor, \lfloor r \sin \theta \rfloor) \\ &= G(m, n; \lfloor r \cos \theta \rfloor + 1, \lfloor r \sin \theta \rfloor) \end{aligned} \quad (6)$$

$$\begin{aligned} G(m, n; r_2, \theta_2) &= G(m, n; \lfloor r \cos \theta \rfloor + 1, \lfloor r \sin \theta \rfloor + 1) \\ &= G(m, n; \lfloor r \cos \theta \rfloor, \lfloor r \sin \theta \rfloor + 1) \end{aligned} \quad (7)$$

$$\begin{aligned} G(m, n; r_3, \theta_3) &= G(m, n; \lfloor r \cos \theta \rfloor + 1, \lfloor r \sin \theta \rfloor + 1) \\ &= G(m, n; \lfloor r \cos \theta \rfloor + 1, \lfloor r \sin \theta \rfloor + 1) \end{aligned} \quad (8)$$

$$\begin{aligned} G(m, n; r_4, \theta_4) &= G(m, n; \lfloor r \cos \theta \rfloor + 1, \lfloor r \sin \theta \rfloor + 1) \\ &= G(m, n; \lfloor r \cos \theta \rfloor + 1, \lfloor r \sin \theta \rfloor + 1) \end{aligned} \quad (9)$$

$$c_1 = (\lfloor r \cos \theta \rfloor + 1 - r \cos \theta) \times (\lfloor r \sin \theta \rfloor + 1 - r \sin \theta) \quad (10)$$

$$c_2 = (r \cos \theta - \lfloor r \cos \theta \rfloor) \times (\lfloor r \sin \theta \rfloor + 1 - r \sin \theta) \quad (11)$$

$$c_3 = (\lfloor r \cos \theta \rfloor + 1 - r \cos \theta) \times (r \sin \theta - \lfloor r \sin \theta \rfloor) \quad (12)$$

$$c_4 = (r \cos \theta - \lfloor r \cos \theta \rfloor) \times (r \sin \theta - \lfloor r \sin \theta \rfloor). \quad (13)$$

The GLCM elements in (6)–(9) (where the last two variables representing relative positions are expressed in the rectangular coordinate system shown in Fig. 1) can be directly calculated using (1), as their corresponding relative positions can coincide with the pixels.

3) *Scheme 3:* Values at arbitrary positions in an image area (i.e., the area occupied by an image in the plane of the image) can be interpolated from values of neighboring pixels. When using interpolations, except nearest-neighbor interpolation, the interpolated values are approximated to integers before calculating GLCM elements.

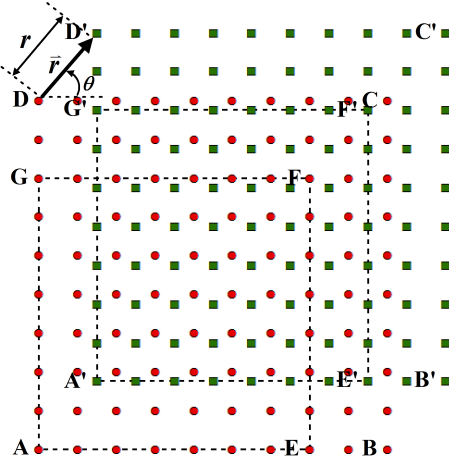


Fig. 2. Geometry of scheme 3 of GLCM calculation.

For convenience, we let the first positions of the position pairs [satisfying the relative position (r, θ) and to be counted] coincide with pixels in the image. The values at the second positions are obtained by interpolation. Then, matrix element (m, n) of the GLCM of the relative position (r, θ) can be calculated by counting the position pairs as

$$G(m, n; r, \theta) = \frac{\text{card} \left\{ \begin{array}{l} (i, j) | f(i, j) = m - 1, \\ f(i + r \cos \theta, j + r \sin \theta) = n - 1, \\ (i, j) \in \mathcal{P}, (i + r \cos \theta, j + r \sin \theta) \in \bar{\mathcal{P}} \end{array} \right\}}{Q(r, \theta)} \quad (14)$$

where $f(i + r \cos \theta, j + r \sin \theta)$ represents the interpolated and rounded value at the second position of the position pair, the first position of which is (i, j) . $\bar{\mathcal{P}}$ denotes the image area. The normalization factor $Q(r, \theta)$ is

$$Q(r, \theta) = \text{card} \{ (i, j) | (i, j) \in \mathcal{P}, (i + r \cos \theta, j + r \sin \theta) \in \bar{\mathcal{P}} \}. \quad (15)$$

For clarity, the first and second positions of the position pairs are illuminated by the geometry in Fig. 2. The pixels of the image are marked by red circles, and the image area ($\bar{\mathcal{P}}$) is the rectangular area ABCD. The first positions are the pixels included in the rectangular area AEFG. The second positions are the first positions displaced by vector \vec{r} [i.e., the relative position (r, θ)], marked by green squares in the rectangular area $A'E'F'G'$.

Alternatively, letting the second positions of the position pairs coincide with the pixels, we can calculate the values at the first positions by interpolation, or those at both first and second positions by interpolation. Then, we can use equations similar to (14) and (15) to count the position pairs to calculate the GLCM.

B. Texture Orientation Estimation

A GLCM is the joint probability distribution of gray levels at the position pairs satisfying a specific relative position within an image. The row and column indexes of the GLCM are gray levels at the two ends of the relative position add 1, and the matrix element at the row and column indexes is

the probability of the position pairs satisfying the relative position and having the corresponding two gray levels at their two ends. Thus, the matrix elements near diagonal line represent probabilities of the position pairs having smaller gray-level differences between their two ends, and those far from the diagonal line represent probabilities of the position pairs having larger gray-level differences.

Gray-level variation along texture orientation is the smallest. Thus, when the parameter of relative orientation (θ) of a GLCM is aligned with the texture orientation, its larger matrix elements are mainly distributed near its diagonal line, as the probabilities of the position pairs having smaller gray-level differences are larger than those of the position pairs having larger gray-level differences. For an ideal line-texture image with no gray-level variation along the texture orientation, only the diagonal line of the GLCM has nonzero matrix elements. For instance, two GLCMs of Fig. 3.1 calculated along and perpendicular to the texture orientation, using different GLCM calculation schemes, and shown in Fig. 4. We can see that in contrast to the GLCM calculated perpendicular to the texture orientation, the GLCM calculated in the texture orientation has larger matrix elements concentrated around its diagonal line.

This property of GLCM provides a cue for extracting texture orientation. This property can be quantitatively parameterized by measuring the degree of concentration of larger elements of a GLCM with respect to its diagonal line as

$$Z(r, \theta) = \sum_{m=1}^N \sum_{n=1}^N w(m, n) \times G(m, n; r, \theta) \quad (16)$$

where $w(m, n)$ is an increasing function of the spacing between matrix element (m, n) and the diagonal line. In this paper, $w(m, n)$ is set to $(m - n)^2$. $Z(r, \theta)$ becomes smaller for higher degrees of concentration.

Once the GLCMs of relative positions equally spaced in distance (r) and orientation (θ) are obtained from the image using one of three GLCM calculation schemes described above, the distribution pattern of $Z(r, \theta)$ is extracted from these GLCMs. Fig. 5 shows the $Z(r, \theta)$ patterns of Fig. 3.1 by the three schemes. We can see that the patterns are consistent with one another, and $Z(r, \theta)$ is mostly small along the texture orientation of Fig. 3.1. Thus, the concentration degrees of larger elements of the GLCMs calculated along the texture orientation are mostly higher than those of the GLCMs calculated along other orientations. However, the texture in Fig. 3.1 has approximate periodicity along nontexture orientations. The gray-level difference between the two ends of a position pair is small, when distance r between the two ends is close to the approximate periodicity along the orientation of that position pair. This causes the minimum values to appear at nontexture orientations in the curve of $Z(r, \theta)$ with respect to θ (keeping r constant). However, these minimum values do not actually correspond to the texture orientation. Therefore, we cannot estimate texture orientation by searching for the minimum values of $Z(r, \theta)$ at a specific constant distance r . To solve this problem, we can use the integral of $Z(r, \theta)$ with respect

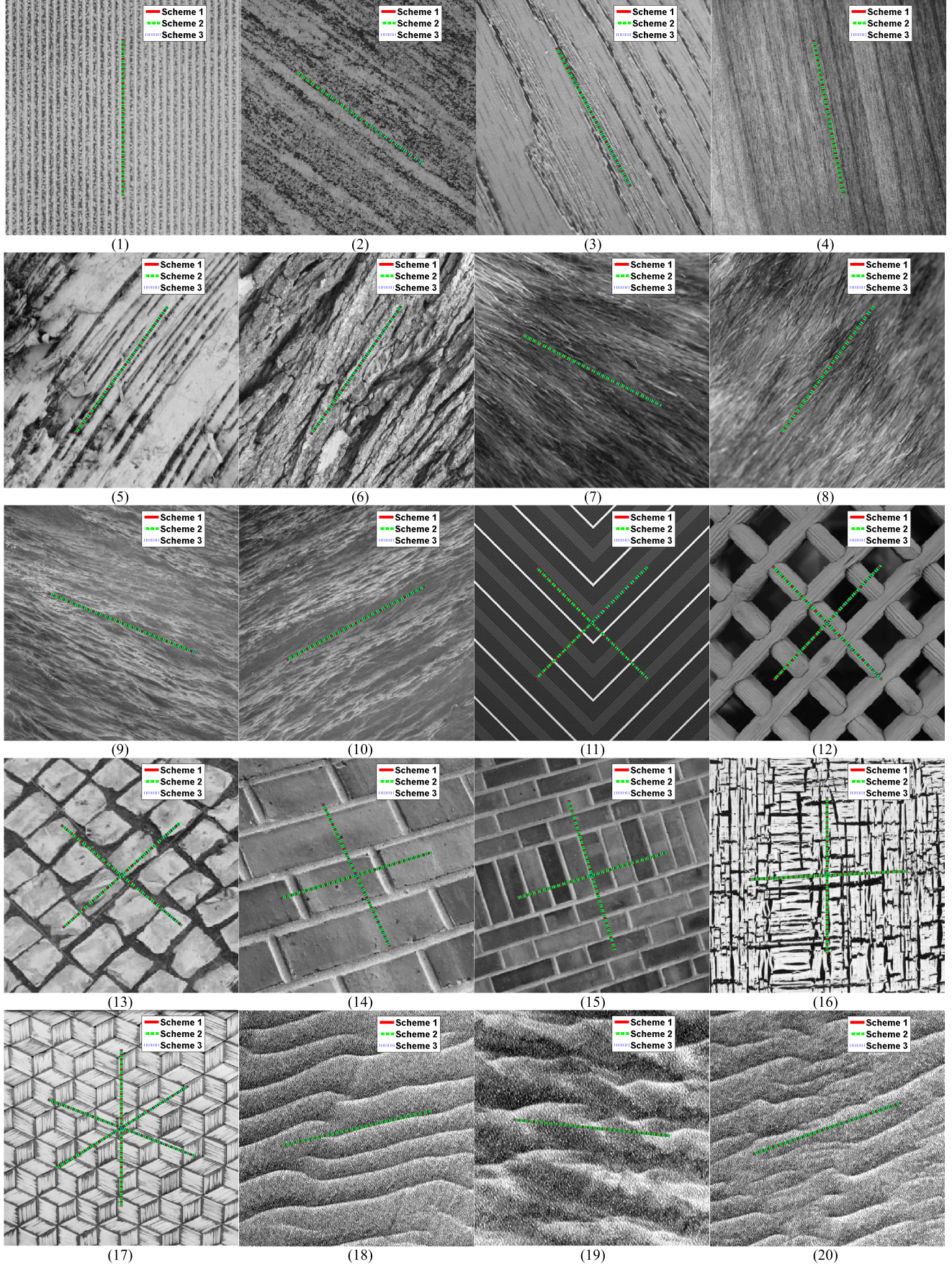


Fig. 3. Texture orientations estimated from the GLCMs (by the three schemes), using the proposed texture orientation estimation method. (1)–(17) photographs and artificial images.

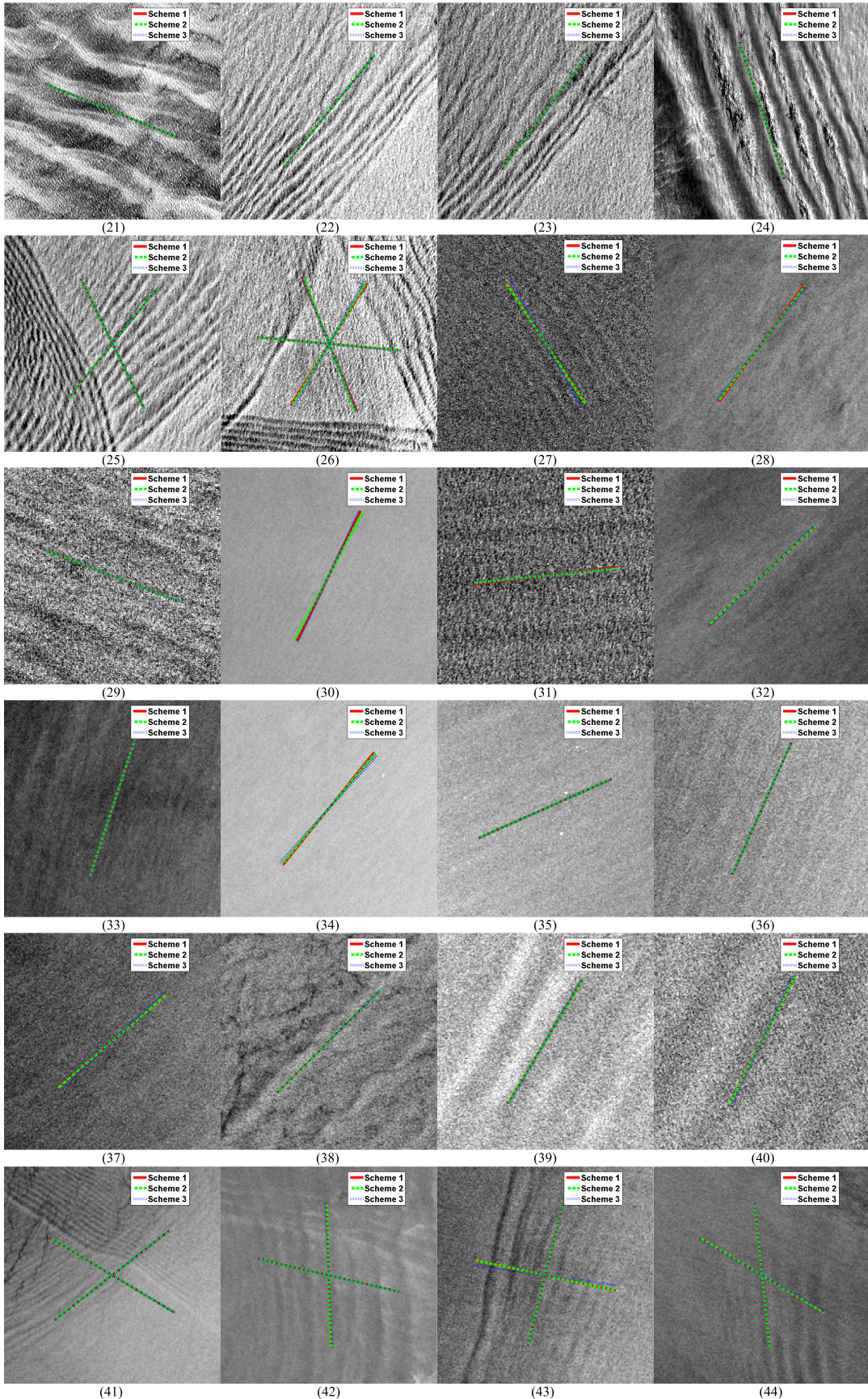


Fig. 3. (Continued.) Texture orientations estimated from the GLCMs (by the three schemes), using the proposed texture orientation estimation method. (18)–(26) optical remote sensing images. (27)–(44) SAR remote sensing images.

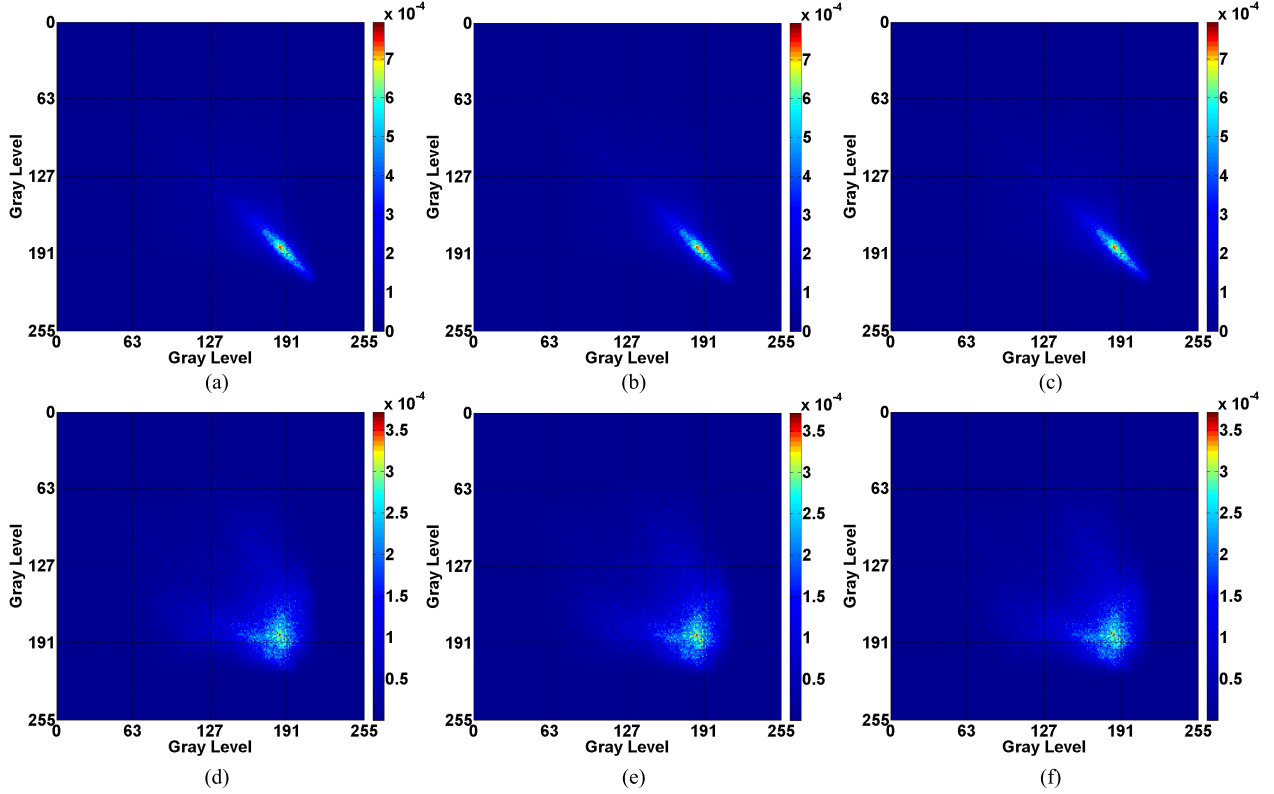


Fig. 4. GLCMs of Fig. 3.1 calculated along the texture orientation and its perpendicular orientation using different schemes. Distance r was 10. (a) Texture orientation, scheme 1. (b) Texture orientation, scheme 2. (c) Texture orientation, scheme 3. (d) Orientation perpendicular to texture orientation, scheme 1. (e) Orientation perpendicular to texture orientation, scheme 2. (f) Orientation perpendicular to texture orientation, scheme 3.

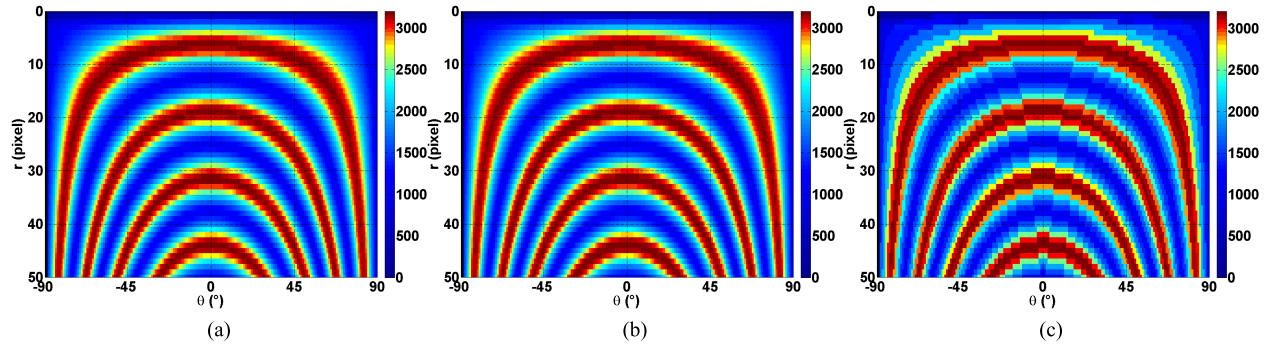


Fig. 5. Z patterns obtained from the GLCMs of Fig. 3.1, calculated by different schemes. (a) Scheme 1. (b) Scheme 2. (c) Scheme 3.

to r instead

$$Z'(\theta) = \int Z(r, \theta) dr. \quad (17)$$

In practical applications, we can use the discrete form of $Z'(\theta)$, such as

$$Z'(\theta) = \sum_{r=1}^R \sum_{m=1}^N \sum_{n=1}^N w(m, n) \times G(m, n; r, \theta) \quad (18)$$

where R is the integration range in (17).

Orientation θ_{\min} corresponding to the minimum value of $Z'(\theta)$ is searched as the dominant texture orientation

$$\theta_{\min} = \arg(\min_{\theta} Z'(\theta)). \quad (19)$$

$Z'(\theta)$ is calculated from $Z(r, \theta)$ of the GLCMs of Fig. 3.1 obtained by the three GLCM calculation schemes. The curves of $Z'(\theta)$ are shown in Fig. 6, normalized by the maximum value of $Z'(\theta)$. These curves were in good agreement with one another, and show that the texture in Fig. 3.1 only has one dominant texture orientation, marked by lines of different colors for different GLCM calculation schemes in Fig. 3.1.

For clarity, Fig. 7 shows the flowchart of this GLCM-based texture orientation estimation method.

III. EXPERIMENTAL RESULTS

A total of 44 images (Fig. 3) including 17 random photographs and artificial images (Fig. 3.1–3.17), 9 optical (Fig. 3.18–3.26), and 18 SAR (Fig. 3.27–3.44) remote sensing

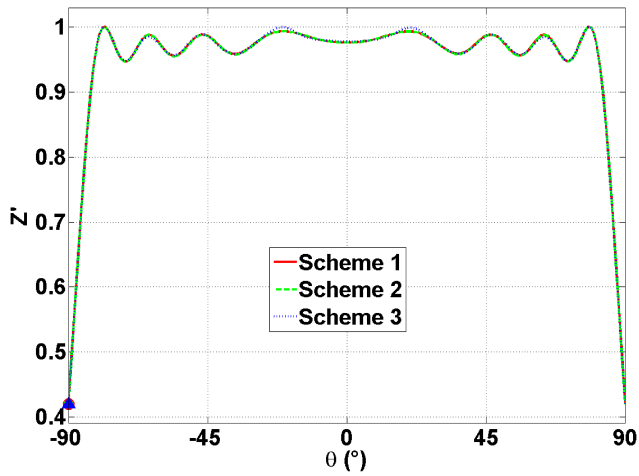


Fig. 6. Z' curves obtained from the GLCMs of Fig. 3.1, calculated by different schemes. (a) Scheme 1. (b) Scheme 2. (c) Scheme 3.

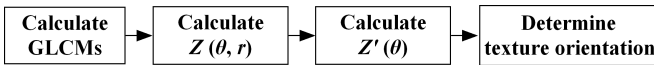


Fig. 7. Flowchart of the GLCM-based texture orientation estimation method.

images were used to test the texture orientation estimation method with the three GLCM calculation schemes. Each image contained 400×400 pixels. The textures in Fig. 3.1–3.10 have only one orientation in each image, including textures of carpet, rock, wood, bark, fur, and water surface. The textures in Fig. 3.11–3.17 have two or three texture orientations in each image, which were used to test the performance of the method in the case of multiple texture orientations. Fig. 3.18–3.44 shows optical and SAR remote sensing images, including signals of sand waves, internal waves, and wind-induced streaks or rolls, which are common oceanic features. They can alter sea surface roughness, modulate electromagnetic and sun glint scattering from the sea surface, and consequently, produce orientated textures in remote sensing images. The SAR images (Fig. 3.27–3.44) were obtained by ENVISAT or Radarsat-2, and the optical images (Fig. 3.18–3.26) were obtained by the Advanced Spaceborne Thermal Emission and Reflection Radiometer onboard the NASA Terra satellite. Nearest-neighbor interpolation was used for the image rotation in scheme 1 of GLCM calculation, and the interpolation step in scheme 3.

A. Comparison Between Scheme 1 of GLCM Calculation and the Conventional Scheme

The three GLCM calculation schemes proposed in the foregoing can be used to calculate the GLCMs of arbitrary relative positions, and thus can be considered as extensions of the conventional scheme [i.e., (1), which can only be used to calculate the GLCMs of relative positions coinciding with pixels]. When calculating the GLCMs of relative positions coinciding with pixels, schemes 2 and 3 are identical to the conventional scheme. The difference is that scheme 1 does not count pixel pairs in the original image, but in the rotated

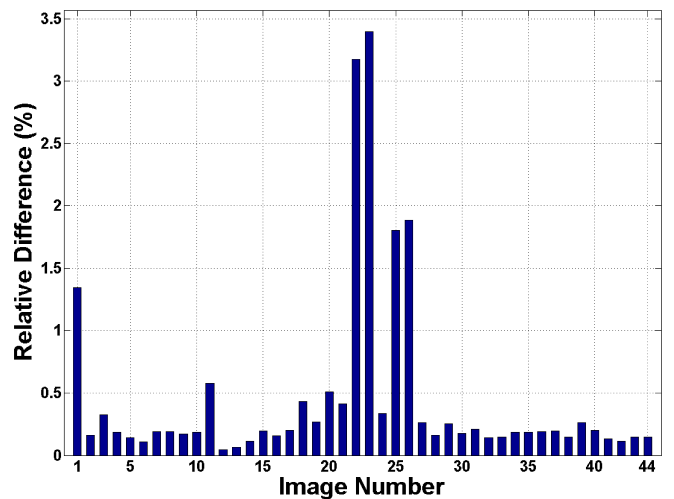


Fig. 8. Relative differences between the values of Z of the GLCMs (calculated by scheme 1 and the conventional scheme) measured by ΔZ_g in (21).

image. In order to examine the consistency of scheme 1 and the conventional scheme in case of relative positions coinciding with the pixels, the following comparison was conducted to investigate the difference in Z between the GLCMs of relative positions coinciding with pixels calculated by scheme 1 and those calculated by the conventional scheme.

The difference $\Delta Z(i, j)$ was calculated, where (i, j) denotes relative position expressed in the rectangular coordinate system shown in Fig. 1

$$\Delta Z(i, j) = Z_1(i, j) - Z_c(i, j). \quad (20)$$

$Z_1(i, j)$ and $Z_c(i, j)$ represent $Z(i, j)$ extracted from the GLCMs of relative position (i, j) , which were calculated using scheme 1 of GLCM calculation and the conventional scheme, respectively. Then, the relative difference was globally measured using ΔZ_g

$$\Delta Z_g = \frac{\sqrt{\sum_{i=-50}^{50} \sum_{j=-50}^{50} \Delta Z(i, j)^2}}{\sqrt{\sum_{i=-50}^{50} \sum_{j=-50}^{50} Z_c(i, j)^2}} \times 100\% \quad (21)$$

which is the ratio of the Frobenius norms of ΔZ and Z_c . The results are given in Fig. 8 for the 44 images shown in Fig. 3. We can see that the relative differences are very small.

B. Comparison Between Method- and Human-Estimated Orientations

The GLCMs of the 44 images of the relative positions equally spaced in terms of orientation (θ) and distance (r) were calculated by the three schemes. The angles (θ) of relative positions varied from -90° to 90° with a 1° increment, and the distances (r) from 1 to 50 with a one-pixel increment. Then, $Z'(\theta)$ was extracted from the GLCMs. The orientations corresponding to the minimum values in $Z'(\theta)$ curves were searched as the dominant texture orientations and marked in Fig. 3. For clarity, these orientations, estimated by the proposed method with different GLCM calculation schemes, are also listed in Table I along with the absolute values (AVs)

TABLE I

TEXTURE ORIENTATIONS ESTIMATED BY GROUP OF 45 PEOPLE AND THE PROPOSED METHOD USING DIFFERENT GLCM CALCULATION SCHEMES

Image Number	Human (°)		Proposed Method with (°)				Image Number	Human (°)		Proposed Method with (°)				
	Mean	SD	Scheme			AV of Max. Diff.		Mean	SD	Scheme			AV of Max. Diff.	
			1	2	3					1	2	3		
1	-89.9	0.6	-90	-90	-90	0	23	52.5	2.6	53	53	53	0	
2	-37.2	2.1	-36	-36	-36	0	24	-71.4	2.3	-72	-72	-72	0	
3	-62.5	2.6	-62	-62	-62	0	25	48.3	5.3	51	51	51	0	
4	-79.0	1.6	-79	-79	-79	0		-64.7	2.3	-64	-64	-64	0	
5	53.4	2.0	54	54	54	0		61.4	4.5	58	59	61	3	
6	56.5	5.2	55	55	55	0	26	-63.4	3.7	-68	-69	-68	1	
7	-37.1	6.1	-27	-27	-27	0		-4.30	2.0	-5	-5	-6	1	
8	53.2	5.1	54	54	54	0		-53.5	5.0	-61	-57	-57	4	
9	-26.3	5.5	-22	-22	-22	0	28	48	4.5	52	53	54	2	
10	28.2	2.8	28	28	28	0	29	-24.8	4.7	-21	-21	-21	0	
11	-45.0	1.4	-45	-45	-45	0	30	58.7	15.8	62	64	65	3	
	44.9	2.1	45	45	45	0	31	4	2.3	6	7	7	1	
12	45.7	1.1	47	47	47	0	32	42.7	4.2	43	43	44	1	
	-44.7	1.6	-46	-46	-46	0	33	69.5	4.9	72	72	72	0	
13	44.8	1.7	42	42	42	0	34	47	5.0	48	50	51	3	
	-41.3	2.8	-40	-40	-40	0	35	30.2	5.3	24	24	24	0	
14	17.1	2.0	17	17	17	0	36	62.5	3.1	66	66	66	0	
	-64.7	1.8	-65	-65	-65	0	37	43.5	4.1	41	41	43	2	
15	16.9	1.5	17	17	17	0	38	46.2	4.4	45	45	45	0	
	-72.1	1.0	-73	-73	-73	0	39	59.6	3.3	59	59	60	1	
16	2.8	2.3	3	3	3	0	40	61.6	3.3	63	63	65	2	
	-89.3	3.4	-90	-90	-90	0	41	35.5	7.0	38	38	38	0	
17	27.4	2.6	32	32	32	0		-31.9	3.5	-32	-31	-31	1	
	-89.4	0.9	-90	-90	-90	0	42	-86.8	3.3	-88	-88	-87	1	
	-24.7	2.6	-21	-21	-21	0		-11.7	6.2	-13	-13	-13	0	
18	10.8	3.0	13	13	13	0	43	76.4	5.7	76	76	76	0	
19	-6.9	6.8	-6	-6	-6	0		-17.5	6.3	-12	-12	-8	4	
20	20.9	3.0	19	19	19	0	44	-27.4	6.1	-31	-31	-30	1	
21	-21.5	5.6	-22	-22	-22	0		-87.9	2.4	-84	-84	-84	0	
22	51.3	3.6	51	51	51	0								

of the maximum orientation differences among them for each image. We can see that the orientations estimated by the proposed method with different GLCM calculation schemes overlapped in most cases in Fig. 3, and the maximum orientation differences among them were very small. (The AVs of the maximum orientation differences were no more than 4°.) Therefore, using (any) one GLCM calculation scheme over the others does not significantly affect the results of the proposed method.

Fig. 3.1, 3.11, 3.12, 3.14, and 3.15 have definite texture orientations, where we can see that the estimated orientations by the method are entirely consistent with them. However, in most cases, texture orientations are ambiguous like the other images in Fig. 3.

Thus, a human visual perception experiment was conducted to crosscheck the results of the texture orientation estimation method. The 44 images (shown in Fig. 3) were given to 45 randomly chosen local college students. They were asked to draw the texture orientations in the paper with rulers and pens. The mean values (MVs) and standard deviations (SDs) of the texture orientations estimated by the 45 students are given in Table I for each image. The MVs are thought to represent the true texture orientations in the images here, and the SDs represent the blurry degrees of the texture orientations. (The higher the blurry degree, the larger is the SD.) For clarity,

Fig. 9 shows the distribution of the SDs. Then, the MV(s) of the texture orientations estimated by the students in each image was used as reference to evaluate the performance of the texture orientation estimation method. The AVs of the differences between the method-estimated and the mean human-estimated orientations are calculated and given in Fig. 10. The differences were found to be very small. Most AVs of the orientation differences were smaller than 3°. The root mean squares (RMSs) of the orientation differences using schemes 1, 2, and 3 were 2.8°, 2.8°, and 3°, which were all smaller than the mean (3.7°) of the SDs of the human-estimated orientations in Table I. Therefore, the texture orientations estimated by the proposed method were in good agreement with those by human visual interpretation.

The SAR images (Fig. 3.27–3.44) contain speckle noise that blurs the texture structures. Correspondingly, texture orientation estimation becomes harder. As shown in Fig. 9, the human-estimated texture orientations of Fig. 3.27–3.44 have larger SDs. This is the reason that objective and subjective retrievals from SAR imagery have larger differences in Fig. 3.27–3.44. This indicates a relationship between SDs and AVs; thus, the correlation between the SDs of the human-estimated orientations and the AVs of the differences between the method-estimated and the mean human-estimated orientations was investigated. Fig. 3.30 was removed as an abnormal

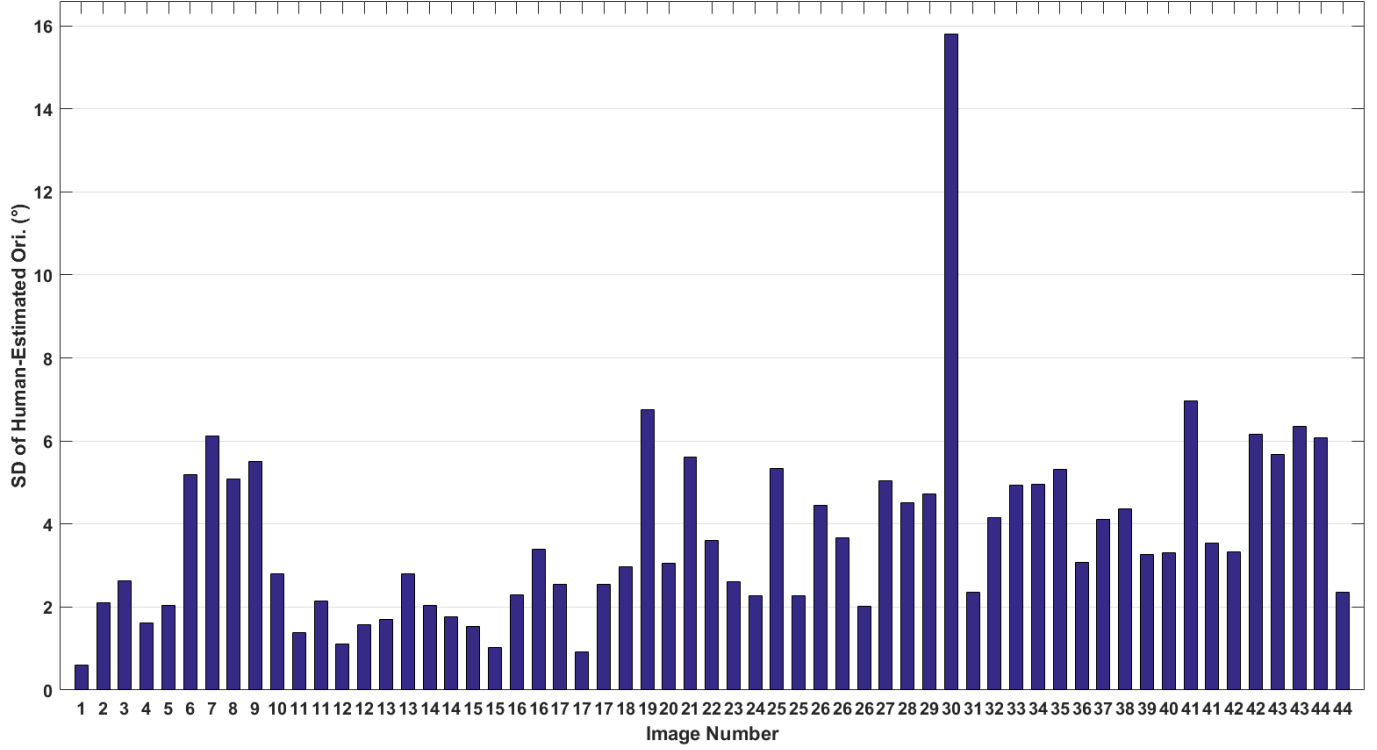


Fig. 9. SDs of texture orientations estimated by 45 people.

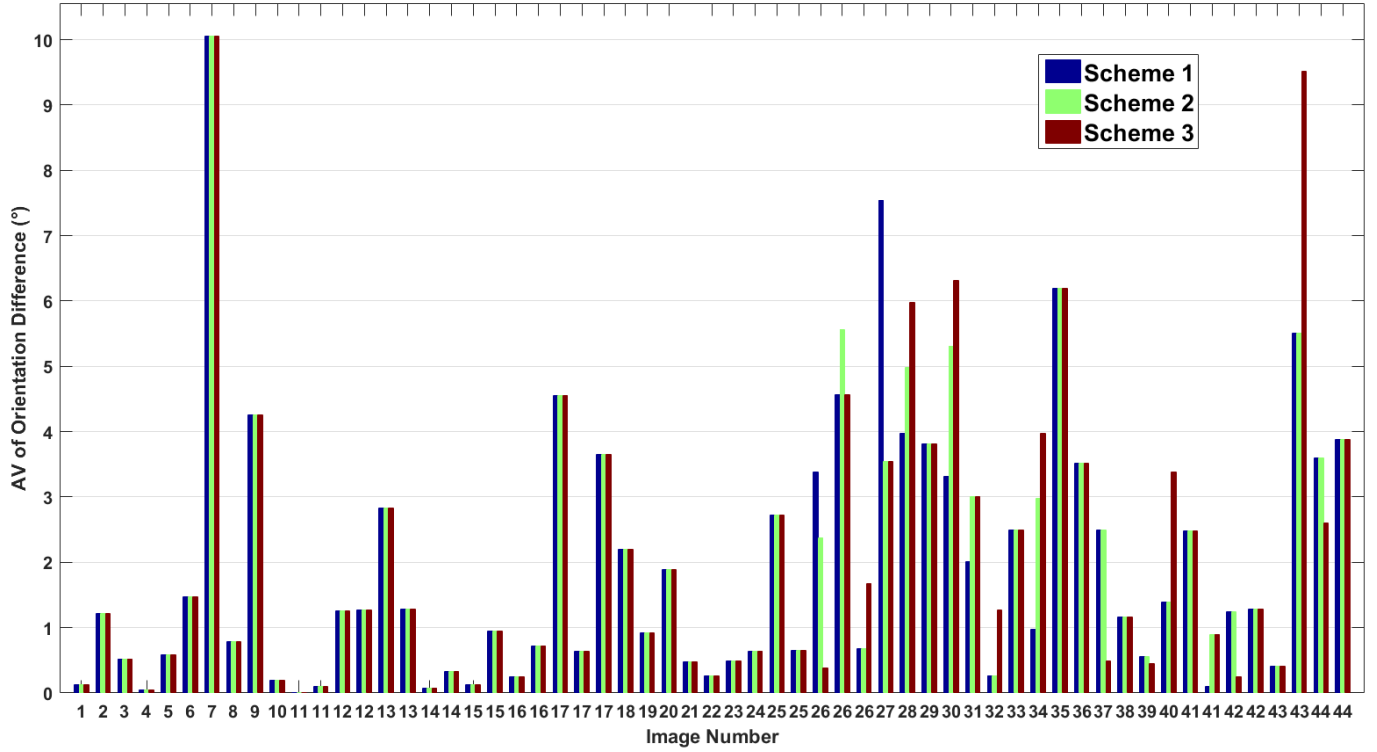


Fig. 10. AVs of differences between the MVs of texture orientations estimated by 45 people and the orientations obtained by the proposed method with schemes 1, 2, and 3.

case in the investigation of the correlation, because it was very blurry and has an exceptionally large SD of human-estimated texture orientations. The correlation coefficients were 0.46,

0.46, and 0.45 between the SDs and the AVs for the proposed method with GLCM calculation schemes 1, 2, and 3; the *p*-values were 3.0E-4, 3.1E-4, and 4.6E-4, which indicate that

TABLE II
INFORMATION ABOUT THE SAR SUBIMAGE DATA SET USED IN THE APPLICATION TEST OF SSWD RETRIEVAL

	Mode	Resolution (m)	VV Number	HH Number	VV+HH Number
Envisat	Image	75×75	35	0	35
	Alternating Polarisation	75×75	23	11	34
	Wide Swath	75×75	4	1	5
Radarsat-2	Fine	5.23 \times 10.71 (before multi-look processing)	0	4	4
		75 \times 75 (after multi-look processing)			
	ScanSAR Narrow	25 \times 25 (before multi-look processing) 75 \times 75 (after multi-look processing)	0	11	11
Total Number			62	27	89

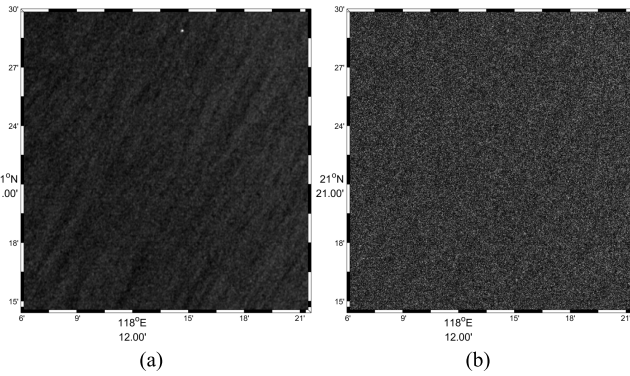


Fig. 11. (a) SAR subimage where wind-induced orientated texture appears. (b) SAR subimage corrupted with speckle noise.

the correlations are significant. Furthermore, it should be noted that the orientation differences of Fig. 3.30 increased insignificantly, compared with those of the other SAR images, and are much smaller than the SD of human-estimated orientations of Fig. 3.30. This means that the proposed method with GLCM calculation schemes 1, 2, and 3 still worked well on this very blurry image.

IV. APPLICATION IN DERIVING SEA SURFACE WIND DIRECTION FROM SAR IMAGERY

Sea surface wind is a critical parameter in affecting atmosphere and ocean circulations, so measurement of both SSWD and sea surface wind speed (SSWS) is very important. For high-resolution sea surface wind mapping with SAR, SSWDs are needed as inputs for SSWS retrieval using an empirical geophysical model function [54]–[57]. Therefore, accurate SSWD also plays an important role for SAR SSWS retrieval.

In this paper, the method developed herein was applied to estimate orientations of wind-induced textures in SAR images to retrieve SSWDs. Then, the results were validated against the ECMWF ERA-Interim reanalysis data [52] and the CCMP data [53]. Interalgorithm comparisons are also made with those commonly used methods based on either the FT [29], [31] or the gradient [47].

The 38 ENVISAT and 3 Radarsat-2 C-band SAR images were collected during February 2004–February 2016, and the methods were applied to their subimages where wind-induced orientated textures appear. Fig. 11(a) shows such a subimage

for example. The 89 subimages were used in this application test. More information about the subimage data set is provided in Table II. The spatial resolution of the ENVISAT subimages is 75 m \times 75 m. The spatial resolution of Radarsat-2 subimages is 5.23 m \times 10.71 m or 25 m \times 25 m, and was transferred into 75 m \times 75 m using multilook processing. The grid size of the CCMP data is 0.25°, and the size of the subimages is about 30 km. Most of the subimages are located between 8°–40° N and 108°–120° E. The range of incidence angle is from 16.85° to 44.06°.

A. Reference Data

The ECMWF ERA-Interim reanalysis data and the CCMP data were used to validate the retrieved SSWDs as reference.

The ECMWF ERA-Interim reanalysis data are generated with data assimilation, advancing forward using 12-h analysis cycles in time. In each cycle, available observations and prior information from a forecast model are combined to obtain the evolving state of the global atmosphere and its underlying surface including u and v wind components at 10 m height on 0.125° grids. The ERA-Interim reanalysis data are provided at times of 0, 6, 12, and 18 UTC.

The CCMP data combine cross-calibrated multiple satellite microwave data with *in situ* data and ECMWF analyses using a 4-D variational analysis method. Each daily data is 0.25° gridded and covers the range from 78.375° S to 78.375° N. u and v wind components at 10 m are also provided at times of 0, 6, 12, and 18 UTC.

The reference data and a SAR subimage were matched as follows. First, the nearest grid of the reference data is found by the center of the subimage. Then, u and v wind components at imaging time are obtained by temporally interpolating the reference data of the nearest two times. Finally, the SSWD is determined from the interpolated u and v wind components.

B. Results

The SSWDs were retrieved from the subimages using the proposed GLCM-based method as well as the FT-based and the gradient-based methods. The 180° ambiguity was removed using ECMWF model wind direction information. Then, the validation results are shown in Figs. 12 and 13 against the ECMWF ERA-Interim reanalysis data and the CCMP data, respectively. The corresponding RMSs of the angle

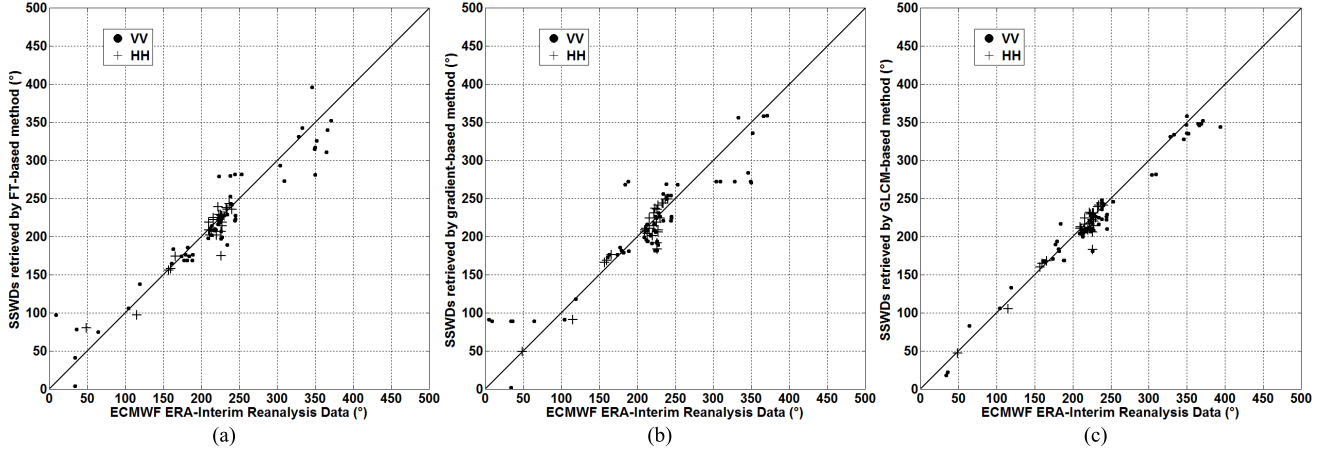


Fig. 12. Scatterplots of the wind directions in the ECMWF ERA-Interim reanalysis data versus those retrieved by the (a) FT-based method, (b) gradient-based method, and (c) proposed GLCM-based method.

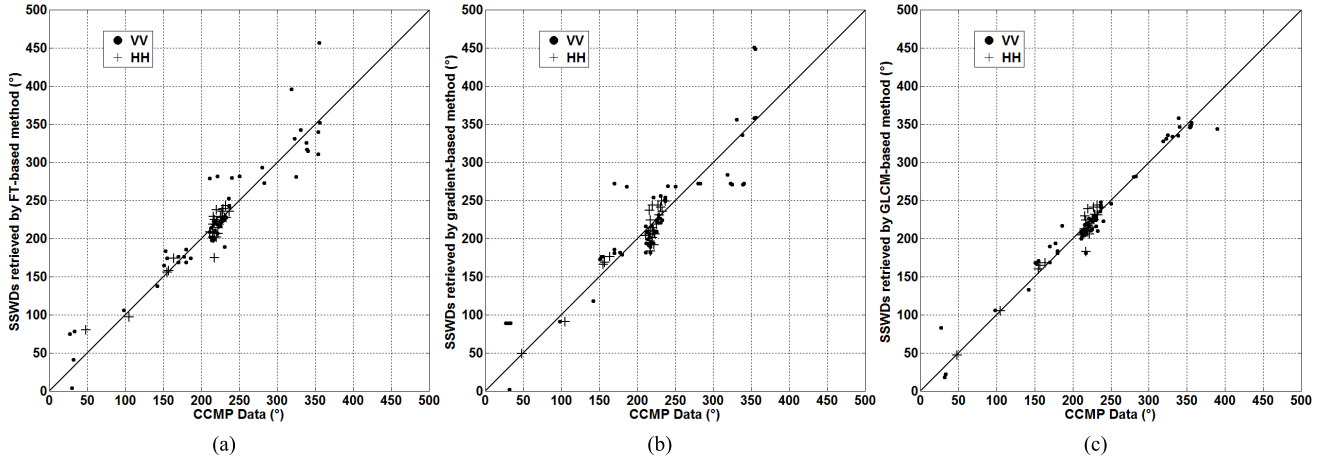


Fig. 13. Scatterplots of the wind directions in the CCMP data versus those retrieved by the (a) FT-based method, (b) gradient-based method, and (c) proposed GLCM-based method.

TABLE III

RMSS OF THE DIFFERENCES BETWEEN THE WIND DIRECTIONS RETRIEVED FROM THE 89 SAR SUBIMAGES BY THE THREE METHODS AND THOSE IN THE ECMWF ERA-INTERIM REANALYSIS DATA

	FT-based method (°)	Gradient-based method (°)	GLCM-based method (°)
VV	25.87	35.71	16.28
HH	14.40	15.19	10.97
Total	23.00	30.96	14.87

TABLE IV

RMSS OF THE DIFFERENCES BETWEEN THE WIND DIRECTIONS RETRIEVED FROM THE 89 SAR SUBIMAGES BY THE THREE METHODS AND THOSE IN THE CCMP DATA

	FT-based method (°)	Gradient-based method (°)	GLCM-based method (°)
VV	26.66	35.30	14.32
HH	13.30	14.54	10.26
Total	23.43	30.53	13.22

differences between the retrieved SSWDs and the reference data are given in Tables III and IV. It should be noted that angle has a period of 360° . Thus, if the AV of an angle difference is larger than 180° , the corresponding retrieved angle should add or subtract 360° . The developed method has good computational efficiency: it takes about 20 s to retrieve SSWD from a subimage (400×400 pixels) using a regular desktop computer (CPU E5-2630 v3 $\times 2$, 2.40 GHz). Although it is not as fast as these less-complex FT- and gradient-based methods, the actual application of the method on remote sensing image processing is acceptable.

From Fig. 12 and Table III, we can see that compared with the results of the other two methods, the results of the

GLCM-based method are closer to the ECMWF ERA-Interim reanalysis data in both vertical–vertical (VV) and horizontal–horizontal (HH) polarized subimages. The RMS of the angle differences in all subimages is smaller than those of the FT- and gradient-based methods by 8.13° and 16.09° .

Fig. 13 and Table IV show the validation results of the retrieved SSWDs against the CCMP data. Overall, the GLCM-based method shows smaller differences in both VV- and HH-polarized subimages, as shown in Fig. 13 and Table IV. The RMS of the angle differences in all subimages is smaller than those of the FT- and gradient-based methods by about 10.21° and 17.31° .

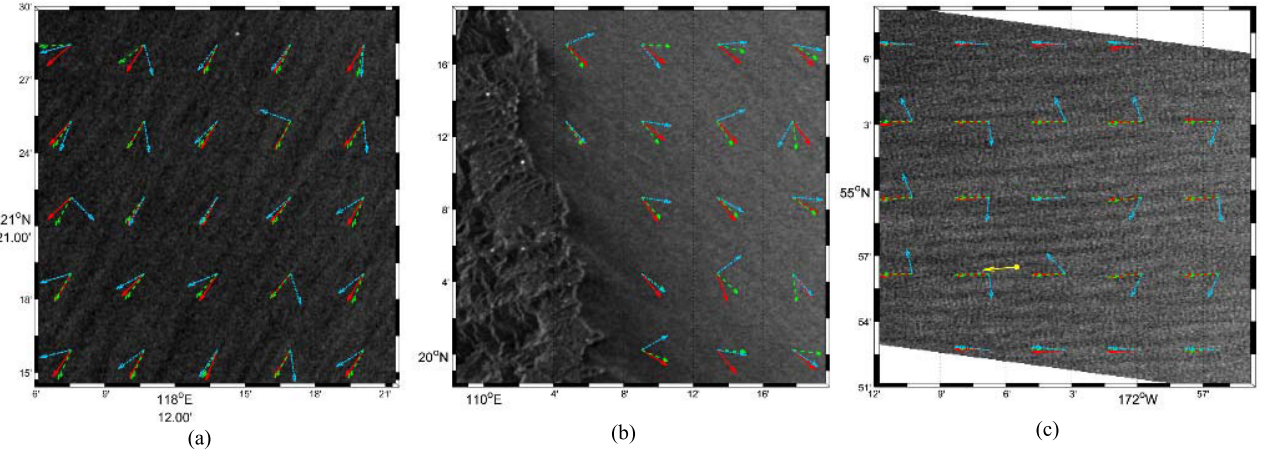


Fig. 14. Wind directions retrieved at 6-km grids by the GLCM-based method (red arrows), the FT-based method (blue arrows), and the gradient-based method (green arrows). (a) ENVISAT image acquired at 02:06 on October 14, 2007. (b) ENVISAT image acquired at 00:45 on March 25, 2005. (c) Radarsat-2 image acquired at 17:58 on February 11, 2011. The yellow dot and arrow in (c) denote the location of the buoy and its measured wind direction.

TABLE V
RMSS OF THE DIFFERENCES BETWEEN THE WIND DIRECTIONS
RETRIEVED FROM THE 89 SPECKLE NOISE-CORRUPTED SAR
SUBIMAGES BY THE THREE METHODS AND THOSE IN THE
REFERENCE DATA

	FT-based method (°)	Gradient-based method (°)	GLCM-based method (°)
ECMWF	42.07	43.38	39.49
CCMP	42.90	43.06	38.90

The speckle noise is common in SAR imagery, which could be modeled using exponential distribution as

$$f'(i, j) = \alpha \times f(i, j). \quad (22)$$

$f(i, j)$ and $f'(i, j)$ are values at position (i, j) in an original image and its speckle noise-corrupted image. α is exponentially distributed random noise with both expectation and variance of 1. Sensitivity to this type of noise was investigated for the applications of the methods in retrieval of SSWDs. All subimages were corrupted with speckle noise. (Actually, these subimages already have speckle noise before this corruption.) Fig. 11(b) shows the speckle noise-corrupted image of Fig. 11(a) as an example. We can see that the wind-induced textures become very blurry after the corruption. Then, the SSWDs were retrieved from the corrupted subimages using different methods. The corresponding RMSS between the results of the methods and the reference data are given in Table V, where we can see that the SSWDs retrieved from these speckle noise-corrupted subimages by the GLCM-based methods are still closer to the reference data than those by the other two methods in both validations against the ECMWF ERA-Interim reanalysis data and the CCMP data.

Three cases are given in Fig. 14 to show the performance of the GLCM-based method to retrieve SSWDs in smaller regions. Among Fig. 14(a)–(c), only Fig. 14(c) coverage contains a National Data Buoy Center buoy location. The SSWD measured by the buoy is denoted by a yellow arrow.

The SSWDs on the grids with sizes of 6 km were retrieved by the GLCM-, FT-, and gradient-based methods and denoted by red, blue, and green arrows in Fig. 14. The texture orientations in Fig. 14(a)–(c) indicate that the general SSWDs are southwestward, southeastward, and southwestward. From Fig. 14, we can see that the FT-based method obviously does not work well. It could be explained by the fact that the FT-based method usually requires a large rectangular data set with many samples of the texture to accurately calculate the Fourier spectrum [40], but the small grids could not meet this requirement well. However, the retrieved SSWDs by the GLCM- and gradient-based methods are consistent with each other and agree with the orientated textures in most grids. On the grids near the buoy in Fig. 14(c), the retrieved SSWDs by the GLCM- and gradient-based methods show obviously better agreement with the measured SSWD than those by the FT-based method.

V. SUMMARY

This paper explored the relationship between texture orientations and GLCMs, and proposed a new method to estimate texture orientations in images. The method is based on the fact found in this paper that larger elements of GLCMs calculated along texture orientations are concentrated near the diagonal lines of the GLCMs. Three schemes were first given to calculate the GLCMs of arbitrary relative positions (i.e., arbitrary orientations and distances) to be used in the proposed texture orientation estimation method. A parameter was then defined to quantitatively measure the degree of concentration of larger elements of a GLCM with respect to its diagonal line. After calculating the GLCMs of the relative positions (equally spaced in terms of orientation and distance) by one of the three GLCM calculation schemes, the distribution pattern of the parameter was extracted. Its integral over the variable of relative distance was selected as an indicator to find the dominant texture orientation(s).

The proposed method with three GLCM calculation schemes was tested using 44 images containing one or multiple aligned textures (including textures of carpet, rock, wood,

bark, fur, and water surface, as well as wave- and wind-induced textures in optical and SAR remote sensing images), and the texture orientations were visually estimated by 45 people as reference. The results of the method with different GLCM calculation schemes were consistent with one another, so using (any) one GLCM calculation scheme over the others does not significantly affect the performance of the method. All method-estimated orientations are in good agreement with human visual inspection. Noise-sensitivity and illumination-sensitivity tests were also conducted. The texture orientations were estimated from the images corrupted by three types of noise (additive Gaussian noise, salt-and-pepper noise, and multiplicative noise) or two changes of illumination, and compared with those from the original images. The results show that the method is insensitive to large typical noises and illumination change.

The application of this GLCM-based texture orientation estimation in retrieval of SSWDs was tested in 89 SAR subimages. Robust automatic extraction of subimages that contain wind-induced textures and distinguishing wind-induced textures from others in SAR images are still a challenge. Some recent progress can be found in [58]. In this paper, the extraction was done visually. Then, this method was used to decide SSWDs objectively. The results were validated against the ECMWF ERA-Interim reanalysis data and the CCMP data. In both cases, the method shows obviously smaller RMSs than do the currently commonly used methods (the FT-based and gradient-based methods) for SSWD retrieval. The sensitivity of the method to the speckle noise, which is common in SAR imagery, was also investigated. The results show that the method is less sensitive to this type of noise than the other two methods. In the case studies of texture-based SSWD retrieval in small regions (6 km), the GLCM- and gradient-based methods are consistent with each other and show better agreement with the wind-induced texture orientations and the buoy measurement than the FT-based method.

This GLCM-based method has broad applications in analyzing aligned features in remote sensing imagery.

APPENDIX

To test the sensitivity of the method to typical noises and illumination change that are common in general image processing, we conducted the following tests.

A. Noise-Sensitivity Test

To evaluate the noise sensitivity of the proposed method, we performed experiments by adding three types of large noise: additive Gaussian, salt-and-pepper, and multiplicative noises. The SAR images already contained large noises, and hence were not involved in the noise-sensitivity and the subsequent illumination-sensitivity tests.

Large Gaussian noise with a signal-to-noise ratio of -10 dB was first added to images from Fig. 3.1–3.26. The texture orientations were then estimated from these additive Gaussian noise-corrupted images by the proposed method with different GLCM calculation schemes, and compared with those estimated from the original images. The RMSs of the

orientation differences were 2.4° , 1.9° , and 2° for the proposed method with schemes 1, 2, and 3.

The original images were then corrupted with salt-and-pepper noise. The ratio of the number of corrupted pixels to the total number of pixels was 50%. The original images were also subsequently corrupted with multiplicative noise. The model of multiplicative noise was

$$f'(i, j) = (1 + \alpha) \times f(i, j) \quad (23)$$

where $f(i, j)$ and $f'(i, j)$ are gray values at position (i, j) in an original image and its multiplicative noise-corrupted image, respectively. α is uniformly distributed random noise with expectation 0 and variance 2. The texture orientations were estimated from the images corrupted by salt-and-pepper noise or multiplicative noise. Afterward, the same comparison was carried out as in the additive Gaussian noise-sensitivity test. For salt-and-pepper noise, the RMSs of the orientation differences were 2.9° , 1.9° , and 1° for the method with schemes 1, 2, and 3 of GLCM calculation. For multiplicative noise, the corresponding RMSs were 2.7° , 2.8° , and 5.4° .

B. Illumination-Sensitivity Test

To test the illumination sensitivity of the proposed method, the illumination of the images (Fig. 3.1–3.26) was changed by multiplying the 2-D Gaussian function as follows:

$$f'(i, j) = \exp \left[-\frac{(i - x)^2 + (j - y)^2}{4w^2} \right] \times f(i, j) \quad (24)$$

where $f(i, j)$ and $f'(i, j)$ are gray values at position (i, j) in an image before and after the illumination change. x and y determined the center of the 2-D Gaussian function, and w determined its width. Two illumination-sensitivity tests were conducted. In the first test, the center of the 2-D Gaussian function was at the center of an image, and the width (w) was 100 (in units of pixels). In the second test, the center was at the bottom-left corner, and the width (w) was 200. The texture orientations were estimated from the illumination-altered images, using the proposed method with different GLCM calculation schemes, and compared with those estimated from the original images without changing illumination. In the first illumination-sensitivity test, the RMSs of the orientation differences were 1.6° , 1.4° , and 1.5° for the proposed method with schemes 1, 2, and 3 of GLCM calculation; in the second illumination-sensitivity test, the RMSs were 2° , 2° , and 2.2° .

The above tests show that the method is insensitive to large typical noises and illumination change.

ACKNOWLEDGMENT

The views, opinions, and findings contained in this paper are those of the authors and should not be construed as an official NOAA or U.S. Government position, policy, and decision.

REFERENCES

- [1] A. Baraldi and F. Parmiggiani, "An investigation of the textural characteristics associated with gray level cooccurrence matrix statistical parameters," *IEEE Trans. Geosci. Remote Sens.*, vol. 33, no. 2, pp. 293–304, Mar. 1995.

- [2] J. Portilla and E. P. Simoncelli, "A parametric texture model based on joint statistics of complex wavelet coefficients," *Int. J. Comput. Vis.*, vol. 40, no. 1, pp. 49–71, Oct. 2000.
- [3] T. N. Pappas, D. L. Neuhoff, H. de Ridder, and J. Zujovic, "Image analysis: Focus on texture similarity," *Proc. IEEE*, vol. 101, no. 9, pp. 2044–2057, Sep. 2013.
- [4] R. M. Haralick, K. Shanmugam, and I. H. Dinstein, "Textural features for image classification," *IEEE Trans. Syst., Man., Cybern.*, vol. SMC-3, no. 6, pp. 610–621, Nov. 1973.
- [5] F. T. Ulaby, F. Kouyate, B. Brisco, and T. H. L. Williams, "Textural information in SAR images," *IEEE Trans. Geosci. Remote Sens.*, vol. GE-24, no. 2, pp. 235–245, Mar. 1986.
- [6] B. Tian, M. A. Shaikh, M. R. Azimi-Sadjadi, T. H. V. Haar, and D. L. Reinke, "A study of cloud classification with neural networks using spectral and textural features," *IEEE Trans. Neural Netw.*, vol. 10, no. 1, pp. 138–151, Jan. 1999.
- [7] R. N. Sutton and E. L. Hall, "Texture measures for automatic classification of pulmonary disease," *IEEE Trans. Comput.*, vol. C-21, no. 7, pp. 667–676, Jul. 1972.
- [8] R. Parekh, "Using texture analysis for medical diagnosis," *IEEE Multi-media*, vol. 19, no. 2, pp. 28–37, Feb. 2010.
- [9] K. R. Krishnan and R. Sudhakar, "Focal and diffused liver disease classification from ultrasound images based on isocontour segmentation," *IET Image Process.*, vol. 9, no. 4, pp. 261–270, Apr. 2015.
- [10] L. H. Siew, R. M. Hodgson, and E. J. Wood, "Texture measures for carpet wear assessment," *IEEE Trans. Pattern Anal. Mach. Intell.*, vol. 10, no. 1, pp. 92–105, Jan. 1988.
- [11] N. Neogi, D. K. Mohanta, and P. K. Dutta, "Review of vision-based steel surface inspection systems," *EURASIP J. Image Video Process.*, vol. 50, Dec. 2014. [Online]. Available: <https://link.springer.com/article/10.1186/1687-5281-2014-50#citeas>, doi: 10.1186/1687-5281-2014-50.
- [12] H. Tamura, S. Mori, and T. Yamawaki, "Textural features corresponding to visual perception," *IEEE Trans. Syst., Man., Cybern.*, vol. SMC-8, no. 6, pp. 460–473, Jun. 1978.
- [13] R. M. Haralick, "Statistical and structural approaches to texture," *Proc. IEEE*, vol. 67, no. 5, pp. 786–804, May 1979.
- [14] V. V. Starovoitov, S.-Y. Jeong, and R.-H. Park, "Texture periodicity detection: Features, properties, and comparisons," *IEEE Trans. Syst., Man., Cybern. A, Syst., Humans*, vol. 28, no. 6, pp. 839–849, Nov. 1998.
- [15] B. Julesz, "Visual pattern discrimination," *IRE Trans. Inf. Theory*, vol. 8, no. 2, pp. 84–92, Feb. 1962.
- [16] B. Julesz, E. N. Gilbert, and L. A. Shepp, "Inability of humans to discriminate between visual textures that agree in second-order statistics—Revisited," *Perception*, vol. 2, no. 4, pp. 391–405, Aug. 1973.
- [17] A. R. Rao and G. L. Lohse, "Identifying high level features of texture perception," *CVGIP, Graph. Model Image Process.*, vol. 55, no. 3, pp. 218–233, May 1993.
- [18] K. S. Friedman and X. Li, "Monitoring hurricanes over the ocean with wide swath SAR," in *Johns Hopkins APL Tech. Dig.*, 2000, vol. 21, no. 1, pp. 80–85.
- [19] C. C. Wackerman *et al.*, "A two-scale model to predict C-band VV and HH normalized radar cross section values over the ocean," *Can. J. Remote Sens.*, vol. 28, no. 3, pp. 367–384, Jun. 2002.
- [20] X. Li, W. Zheng, W. G. Pichel, C.-Z. Zou, and P. Clemente-Colón, "Coastal katabatic winds imaged by SAR," *Geophys. Res. Lett.*, vol. 34, no. 3, pp. 300–315, Feb. 2007.
- [21] X. Yang, X. Li, Q. Zheng, X. Gu, W. G. Pichel, and Z. Li, "Comparison of ocean-surface winds retrieved from QuikSCAT scatterometer and Radarsat-1 SAR in offshore waters of the U.S. West Coast," *IEEE Geosci. Remote Sens. Lett.*, vol. 8, no. 1, pp. 163–167, Jan. 2011.
- [22] B. Zhang *et al.*, "Ocean vector winds retrieval from c-band fully polarimetric SAR measurements," *IEEE Trans. Geosci. Remote Sens.*, vol. 50, no. 11, pp. 4252–4261, Nov. 2012.
- [23] X. Zhou *et al.*, "Estimation of tropical cyclone parameters and wind fields from SAR images," *Sci. China, Earth Sci.*, vol. 56, no. 11, pp. 1977–1987, Jun. 2013.
- [24] G. Liu *et al.*, "A systematic comparison of the effect of polarization ratio models on sea surface wind retrieval from c-band synthetic aperture radar," *IEEE J. Sel. Topics Appl. Earth Observ. Remote Sens.*, vol. 6, no. 3, pp. 1100–1108, Jun. 2013.
- [25] T. S. Kim, K.-A. Park, X. Li, and S. Hong, "SAR-derived wind fields at the coastal region in the East/Japan Sea and relation to coastal upwelling," *Int. J. Remote Sens.*, vol. 35, nos. 11–12, pp. 3947–3965, May 2014.
- [26] G. Zhang, W. Perrie, X. Li, and J. A. Zhang, "A hurricane morphology and sea surface wind vector estimation model based on C-band cross-polarization SAR imagery," *IEEE Trans. Geosci. Remote Sens.*, vol. 55, no. 3, pp. 1743–1751, Mar. 2017.
- [27] G. Mastin, C. Harlow, O. Huh, and S. Hsu, "Methods of obtaining offshore wind direction and sea-state data from X-band aircraft SAR imagery of coastal waters," *IEEE J. Ocean. Eng.*, vol. OE-10, no. 2, pp. 159–174, Apr. 1985.
- [28] D. Etling and R. A. Brown, "Roll vortices in the planetary boundary layer: A review," *Boundary Layer Meteorol.*, vol. 65, no. 3, pp. 215–248, Aug. 1993.
- [29] C. C. Wackerman, C. L. Rufenach, R. A. Shuchman, J. A. Johannessen, and K. L. Davidson, "Wind vector retrieval using ERS-1 synthetic aperture radar imagery," *IEEE Trans. Geosci. Remote Sens.*, vol. 34, no. 6, pp. 1343–1352, Nov. 1996.
- [30] T. D. Sikora and G. S. Young, "Wind-direction dependence of quasi-2D SAR signatures," in *Proc. IEEE Int. Geosci. Remote Sens. Symp.*, Toronto, ON, Canada, Jun. 2002, pp. 1887–1889.
- [31] J. Horstmann and W. Koch, "Measurement of ocean surface winds using synthetic aperture radars," *IEEE J. Ocean. Eng.*, vol. 30, no. 3, pp. 508–515, Jul. 2005.
- [32] W. Alpers, "Theory of radar imaging of internal waves," *Nature*, vol. 314, pp. 245–247, Mar. 1985.
- [33] H. Shao, Y. Li, and L. Li, "Sun glitter imaging of submarine sand waves on the Taiwan Banks: Determination of the relaxation rate of short waves," *J. Geophys. Res.*, vol. 116, no. C6, Jun. 2011. [Online]. Available: <http://onlinelibrary.wiley.com/doi/10.1029/2010JC006798/full#footer-citing>, doi: 10.1029/2010JC006798.
- [34] K. Yang *et al.*, "Observation of submarine sand waves using ASTER stereo sun glitter imagery," *Int. J. Remote Sens.*, vol. 36, no. 22, pp. 5576–5592, Oct. 2015.
- [35] M. A. Simaan, "Artificial neural network classification of texture orientations in seismic images," in *Proc. IEEE Conf. Image Process.*, vol. 1, Barcelona, Spain, Sep. 2003, pp. I-281–I-284.
- [36] A. Marion and D. Vray, "Spatiotemporal filtering of sequences of ultrasound images to estimate a dense field of velocities," *Pattern Recognit.*, vol. 42, no. 11, pp. 2989–2997, Nov. 2009.
- [37] B. Josso, D. R. Burton, and M. J. Lalor, "Texture orientation and anisotropy calculation by Fourier transform and Principal Component Analysis," *Mech. Syst. Signal Process.*, vol. 19, no. 5, pp. 1152–1161, Sep. 2005.
- [38] D. V. S. Chandra, "Target orientation estimation using Fourier energy spectrum," *IEEE Trans. Aerosp. Electron. Syst.*, vol. 34, no. 3, pp. 1009–1012, Jul. 1998.
- [39] J. Bigun, G. H. Granlund, and J. Wiklund, "Multidimensional orientation estimation with applications to texture analysis and optical flow," *IEEE Trans. Pattern Anal. Mach. Intell.*, vol. 13, no. 8, pp. 775–790, Aug. 1991.
- [40] A. Source, G. Plantier, and J.-L. Saumet, "Autocorrelation fitting for texture orientation estimation," in *Proc. IEEE Conf. Image Process.*, vol. 1, Barcelona, Spain, Sep. 2003, pp. I-281–I-284.
- [41] K. Jafari-Khouzani and H. Soltanian-Zadeh, "Radon transform orientation estimation for rotation invariant texture analysis," *IEEE Trans. Pattern Anal. Mach. Intell.*, vol. 27, no. 6, pp. 1004–1008, Jun. 2005.
- [42] M. Ceccarelli, M. De Filippo, M. Di Bisceglie, and C. Galdi, "A texture based approach for ocean surface wind detection in SAR images," in *Proc. IEEE Int. Workshop Imag. Syst. Techn.*, Crete, Greece, Sep. 2008, pp. 193–197.
- [43] J. Zhang, X. Mai, and X. Wu, "Rotation invariant texture classification with dominant orientation estimation based on Gabor filters," in *Proc. IEEE Conf. Comput. Sci. Autom. Eng.*, vol. 1, Shanghai, China, Jun. 2011, pp. 606–609.
- [44] A. Lefebvre, T. Corpetti, and L. H. Moy, "Estimation of the orientation of textured patterns via wavelet analysis," *Pattern Recognit. Lett.*, vol. 32, no. 2, pp. 190–196, Jan. 2011.
- [45] A. R. Rao, *A Taxonomy for Texture Description and Identification*. New York, NY, USA: Springer-Verlag, 1990.
- [46] B. B. Chaudhuri, P. Kundu, and N. Sarkar, "Detection and gradation of oriented texture," *Pattern Recognit.*, vol. 14, no. 2, pp. 147–153, Feb. 1993.
- [47] W. Koch, "Directional analysis of SAR images aiming at wind direction," *IEEE Trans. Geosci. Remote Sens.*, vol. 42, no. 4, pp. 702–710, Apr. 2004.
- [48] F. L. Pouliquen, J.-P. D. Costa, C. Germain, and P. Baylou, "A new adaptive framework for unbiased orientation estimation in textured images," *Pattern Recognit.*, vol. 38, no. 11, pp. 2032–2046, Nov. 2005.

- [49] M. M. Islam, D. Zhang, and G. Lu, "A geometric method to compute directionality features for texture images," in *Proc. IEEE Conf. Multimedia Expo.*, Hannover, Germany, Jun. 2008, pp. 1521–1524.
- [50] L. Zhou *et al.*, "An improved local gradient method for sea surface wind direction retrieval from SAR imagery," *Remote Sens.*, vol. 9, no. 7, p. 671, Jun. 2017, doi: [10.3390/rs9070671](https://doi.org/10.3390/rs9070671).
- [51] R. Mester, "Orientation estimation: Conventional techniques and a new non-differential approach," in *Proc. 10th Eur. Signal Process. Conf.*, Tampere, Finland, Sep. 2000, pp. 1–4.
- [52] D. P. Dee *et al.*, "The ERA-Interim reanalysis: Configuration and performance of the data assimilation system," *Quart. J. Roy. Meteorol. Soc.*, vol. 137, pp. 553–597, Apr. 2011.
- [53] R. Atlas *et al.*, "A cross-calibrated, multiplatform ocean surface wind velocity product for meteorological and oceanographic applications," *Bull. Amer. Meteorol. Soc.*, vol. 92, no. 2, pp. 157–174, Feb. 2011.
- [54] Q. Xu *et al.*, "Assessment of an analytical model for sea surface wind speed retrieval from spaceborne SAR," *Int. J. Remote Sens.*, vol. 31, no. 4, pp. 993–1008, Feb. 2010.
- [55] X. Yang, X. Li, W. G. Pichel, and Z. Li, "Comparison of ocean surface winds from ENVISAT ASAR, MetOp ASCAT scatterometer, buoy measurements, and NOGAPS model," *IEEE Trans. Geosci. Remote Sens.*, vol. 49, no. 12, pp. 4743–4750, Dec. 2011.
- [56] F. M. Monaldo *et al.*, "Ocean wind speed climatology from spaceborne SAR imagery," *Bull. Amer. Meteorol. Soc.*, vol. 95, no. 4, pp. 565–569, Jun. 2014.
- [57] F. M. Monaldo, C. R. Jackson, X. Li, and W. G. Pichel, "Preliminary evaluation of Sentinel-1A wind speed retrievals," *IEEE J. Sel. Topics Appl. Earth Observ. Remote Sens.*, vol. 9, no. 6, pp. 2638–2642, Jun. 2016.
- [58] C. T. Jones, T. D. Sikora, P. W. Vachon, J. Wolfe, and B. DeTracey, "Automated discrimination of certain brightness fronts in RADARSAT-2 images of the ocean surface," *J. Atmos. Ocean. Technol.*, vol. 30, no. 9, pp. 2203–2215, Sep. 2013.



Gang Zheng received the B.S. degree in electronic information engineering from Zhejiang University, Hangzhou, China, in 2003, and the M.S. and Ph.D. degrees in radio physics from the University of Electronic Science and Technology of China, Chengdu, China, in 2006 and 2010, respectively.

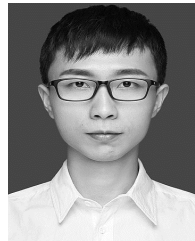
From 2010 to 2013, he was an Assistant Researcher with the State Key Laboratory of Satellite Ocean Environment Dynamics, Second Institute of Oceanography, State Oceanic Administration, Hangzhou, where he has been an Associate Researcher since 2013. His research interests include ocean microwave remote sensing, image processing, and electromagnetic numerical modeling.



Xiaofeng Li (M'00-SM'11) received the B.S. degree in optical engineering from Zhejiang University, Hangzhou, China, in 1985, the M.S. degree in physical oceanography from the First Institute of Oceanography, State Oceanic Administration, Qingdao, China, in 1992, and the Ph.D. degree in physical oceanography from North Carolina State University, Raleigh, NC, USA, in 1997.

During the M.S. program, he completed the graduate course work from the Department of Physics, University of Science and Technology of China, Hefei, China. Since 1997, he has been with the National Environmental Satellite, Data, and Information Service (NESDIS), NOAA, College Park, MD, USA, where he is involved in developing many operational satellite ocean remote sensing products. He has authored over 100 peer-reviewed publications and edited three books. His research interests include remote sensing oceanography and marine meteorology, satellite image processing, oil spill and coastal zone classification with multipolarization synthetic aperture radars, and the development of sea surface temperature algorithms.

Dr. Li received the Individual Award for Science from the NOAA/NESDIS Center for Satellite Applications and Research, the Len Curtis Award from the Remote Sensing and Photogrammetry Society, and the Overseas Expert Title from the Chinese Academy of Sciences. He is an Associate Editor of the *IEEE TRANSACTIONS ON GEOSCIENCE AND REMOTE SENSING* and the *International Journal of Remote Sensing*, the Ocean Section Editor-in-Chief of *Remote Sensing*, and an Editorial Board Member of the *International Journal of Digital Earth and Big Earth Data*.



Lizhang Zhou received the B.S. degree in physics from Nanjing University, Nanjing, China, in 2015. He is currently pursuing the master's degree with the Second Institute of Oceanography, State Oceanic Administration, Hangzhou, China.

His research interests include ocean microwave remote sensing.



Jingsong Yang received the B.S. degree in physics and the M.S. degree in theoretical physics from Zhejiang University, Hangzhou, China, in 1990 and 1993, respectively, and the Ph.D. degree in physical oceanography from the Ocean University of China, Qingdao, China, in 2001.

Since 1996, he has been with the Second Institute of Oceanography (SIO), State Oceanic Administration, Hangzhou, where he is currently the Head of the microwave marine remote sensing with the State Key Laboratory of Satellite Ocean Environment Dynamics. Since 2002, he has been a Supervisor of graduate students with SIO, and since 2011, he has been an Adjunct Professor and a Doctoral Supervisor with Zhejiang University. He has more than 19 years' experience in microwave marine remote sensing. He has been a Principal Investigator and a Participant in more than 20 research projects. He has authored over 100 scientific papers in peer-reviewed journals and international conference proceedings. His research interests include microwave marine remote sensing, data fusion, image processing, and satellite oceanography.

Dynamics. Since 2002, he has been a Supervisor of graduate students with SIO, and since 2011, he has been an Adjunct Professor and a Doctoral Supervisor with Zhejiang University. He has more than 19 years' experience in microwave marine remote sensing. He has been a Principal Investigator and a Participant in more than 20 research projects. He has authored over 100 scientific papers in peer-reviewed journals and international conference proceedings. His research interests include microwave marine remote sensing, data fusion, image processing, and satellite oceanography.



Lin Ren received the B.S. degree in electronic information engineering from the Anhui University of Science and Technology, Huainan, China, in 2005, and the Ph.D. degree in microwave remote sensing from the Nanjing University of Science and Technology, Nanjing, China, in 2011.

He is currently an Associate Researcher with the State Key Laboratory of Satellite Ocean Environment Dynamics, Second Institute of Oceanography, State Oceanic Administration, Hangzhou, China. His research interests include ocean microwave remote sensing and satellite oceanography.

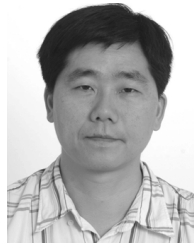


Peng Chen was born in Anren, Hunan, China. He received the M.S. degree in physical oceanography from the Second Institute of Oceanography (SIO), State Oceanic Administration (SOA), Hangzhou, China, in 2004, and the Ph.D. degree in geographic information system from Zhejiang University, Hangzhou, in 2011.

He is currently an Associate Researcher in marine remote sensing with the State Key Laboratory of Satellite Ocean Environment Dynamics, SIO, SOA, focusing on the development of algorithms detecting marine targets (ship, oil rig, and oil slick).



Huaguo Zhang is currently a Researcher with the State Key Laboratory of Satellite Ocean Environment Dynamics, Second Institute of Oceanography, State Oceanic Administration, Hangzhou, China. He has authored over 40 papers in international peer-reviewed journals and proceedings. His research interests include the coastal remote sensing and ocean sun glint remote sensing.



Xiulin Lou received the Ph.D. degree in remote sensing and satellite oceanography from the Ocean University of China, Qingdao, China, in 2011.

He is currently a Researcher with the State Key Laboratory of Satellite Ocean Environment Dynamics, Second Institute of Oceanography, State Oceanic Administration, Hangzhou, China. His research interests include remote sensing of red tides, sea surface currents, and coastal environments.